

Practical human abdominal fat imaging utilizing electrical impedance tomography

This article has been downloaded from IOPscience. Please scroll down to see the full text article.

2010 Physiol. Meas. 31 963

(<http://iopscience.iop.org/0967-3334/31/7/007>)

View [the table of contents for this issue](#), or go to the [journal homepage](#) for more

Download details:

IP Address: 133.20.132.125

The article was downloaded on 16/06/2010 at 11:04

Please note that [terms and conditions apply](#).

Practical human abdominal fat imaging utilizing electrical impedance tomography

T Yamaguchi¹, K Maki^{2,3} and M Katashima¹

¹ Health Care Food Research Laboratories, Kao Corporation, 2-1-3 Bunka Sumida Tokyo, 131-8501, Japan

² Processing Development Research Laboratories, Kao Corporation, 2606 Akabane Ichikai-machi Haga Tochigi, 321-3497, Japan

E-mail: yamaguchi.tohru@kao.co.jp

Received 1 December 2009, accepted for publication 26 May 2010

Published 15 June 2010

Online at stacks.iop.org/PM/31/963

Abstract

The fundamental cause of metabolic syndrome is thought to be abdominal obesity. Accurate diagnosis of abdominal obesity can be done by an x-ray computed tomography (CT) scan. But CT is expensive, bulky and entails the risks involved with radiation. To overcome such disadvantages, we attempted to develop a measuring device that could apply electrical impedance tomography to abdominal fat imaging. The device has 32 electrodes that can be attached to a subject's abdomen by a pneumatic mechanism. That way, electrode position data can be acquired simultaneously. An applied alternating current of 1.0 mA was used at a frequency of 500 kHz. Sensed voltage data were carefully filtered to remove noise and processed to satisfy the reciprocal theorem. The image reconstruction software was developed concurrently, applying standard finite element methods and the Marquardt method to solve the mathematical inverse problem. The results of preliminary experiments showed that abdominal subcutaneous fat and the muscle surrounding the viscera could be imaged in humans. While our imaging of visceral fat was not of sufficient quality, it was suggested that we will be able to develop a safe and practical abdominal fat scanner through future improvements.

Keywords: abdominal obesity, visceral fat, bioimpedance, tomography, finite element method, inverse problem, singular value decomposition, nonlinear optimization, Marquardt method

³ Present address: Clinic Saint Louis, Kyoto, Japan.

1. Introduction

Metabolic syndrome is a disease state related to lifestyles such as dietary habits and exercise, and is becoming a significant health problem worldwide. A fundamental cause of metabolic syndrome is thought to be abdominal obesity (Després and Lemieux 2006) which is mainly the accumulation of visceral fat. Therefore, the importance of managing visceral fat has been emphasized in guidelines for the management of metabolic syndrome (Grundy *et al* 2005, Matsuzawa 2005).

To manage visceral fat, it is necessary to estimate its volume. A possible estimation method in the screening stage of the diagnosis is to measure the waist circumference, but that has been criticized from the viewpoint of clinical usefulness (Klein *et al* 2007). While dual-x-ray absorptiometry (DXA) is becoming popular as a diagnosis method for the body fat (Genton *et al* 2002) that cannot derive cross-sectional image of the abdomen, we cannot distinguish between visceral fat obesity which is more important clinically and abdominal subcutaneous fat obesity. Therefore, x-ray computed tomography (CT) or magnetic resonance imaging is employed for a more accurate diagnosis. But the apparatus involved in both methods is expensive and require a large space; thus, it is difficult to introduce them into small clinics. Furthermore, in the case of x-ray CT, the radiation involved raises concerns about its safety (Brenner and Hall 2007) for diagnosis, especially if the patient is a child or potentially pregnant woman.

The above issues are the reasons why a smaller, more inexpensive, safer device for visceral fat quantitation is in demand. In Japan, 'The Japanese National Health Screening and Intervention Program Aimed at Preventing Worsening of the Metabolic Syndrome' commenced in 2008 (Kohro *et al* 2008). To screen for patients with a high risk for metabolic syndrome, a practical, safe device with the accuracy of x-ray CT is needed.

The bioimpedance method for body fat estimation is one of the safer methods available (Kushner 1992). It utilizes the fact that body fat has characteristically low electric conductivity. A device to estimate abdominal fat which involves attaching electrodes to the abdomen has been in development. Scharfetter *et al* studied extensively the four-electrode system, but they achieved good estimation only for abdominal subcutaneous fat (Scharfetter *et al* 2005, 2001). Ryo *et al* studied a similar but different electrode-placement system focusing on visceral fat (Ryo *et al* 2005, Watson *et al* 2009), but it still lacks the necessary accuracy as a device for medical diagnosis. The authors contributed to this work partially.

Thus, we propose the application of electrical impedance tomography (EIT) (Holder 2005a, Boone *et al* 1997) as a practical solution. In the present study, we attempted to develop a measuring device as accurate as x-ray CT using abdominal electrical conductivity imaging by EIT.

2. Method: apparatus for impedance measurement

2.1. Mechanical design

The developed device was not designed for severely ill patients, but rather for subjects who could be measured in the upright position. The frame of the device was composed of aluminum. The size (width × depth × height) was 890 mm × 1175 mm × 1440 mm. The device was equipped with a small air compressor for the pneumatic system; thus, it needed only 100 V of electric power for the energy source. Therefore, it could be moved through an ordinary door and installed anywhere in hospitals (figure 1).

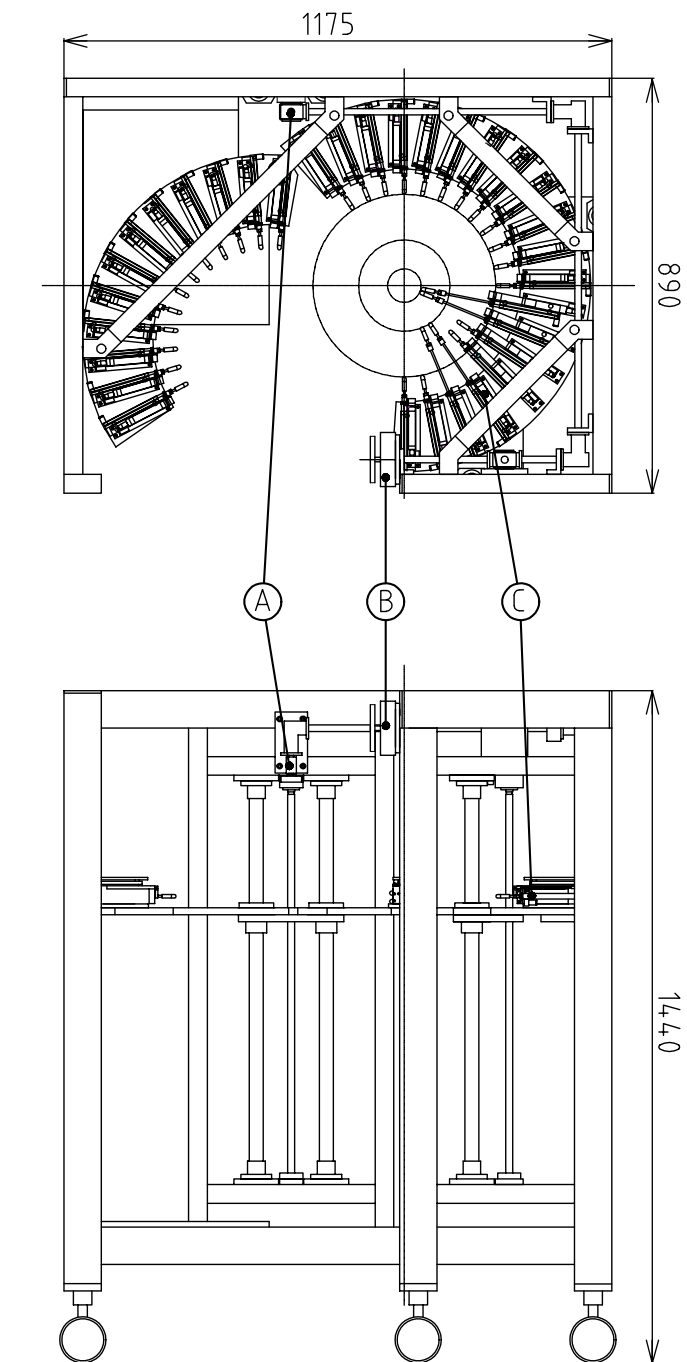


Figure 1. Drawing of the device in top view and side view. Unit of length is millimeters. (A) A ball screw to sustain the electrode units; (B) a rotating handle to adjust the level of electrodes; and (C) an electrode unit.

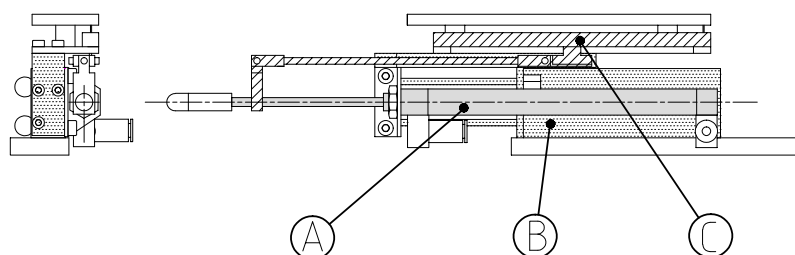


Figure 2. Drawing of the electrode. (A) Second-stage cylinder; (B) first-stage cylinder, and (C) a slide potentiometer and the linkage.

We designed a special semi-automatic electrode-attaching system utilizing a pneumatic mechanism controlled by a personal computer (PC) since the manual attachment of electrodes is generally very time consuming. The level of electrodes was adjustable in the range of 850–1250 mm above the floor. The maximum diameter of measurement was 410 mm; thus, a subject who is suspected of metabolic syndrome with a waist circumference of around 90 cm could be imaged.

Electrodes were made of stainless steel, hemispherical in shape and were pushed by air cylinders. To take a long stroke in a narrow space, the mechanism had a double action: a 60 mm stroke cylinder in the first stage and 75 mm stroke cylinder in the second stage. In the second-stage cylinder, we introduced an ultra-low friction cylinder (Airpel, Airpot Corporation, Norwalk, CT); thus, gentle pushing and smooth movement of electrodes were achieved. Furthermore, the rods of the second-stage cylinder were linked mechanically to a low-friction slide potentiometer, which could measure the position of the rods. Therefore, the outline of the abdomen could be measured (figure 2).

2.2. Electronic circuits

The electronic circuits were composed of both an originally designed part and commercially available instruments as shown in figure 3. Those circuits were installed on the small free space inside the outer frame. All of the instruments were controlled by a PC through a GP-IB interface.

The electric current source was composed of a sine wave generator (Agilent33120A, Agilent Technologies, Santa Clara, CA) and an original push-pull type constant current circuit. Its two outputs were connected to matrix switches (Agilent34904A, Agilent Technologies, Santa Clara, CA) that could be connected to any electrode. The frequency and amplitude of the generated current were adjustable in the range of 10–500 kHz, and 0.1–2.0 mA, respectively.

Injecting current through two electrodes generated a potential difference depending on the bioimpedance distribution of the subject's abdomen and could be measured by two other adjacent electrodes. This signal was amplified and its common mode component was removed by differential amplifiers. The outputs of those amplifiers were connected to a multiplexer (Agilent34902A, Agilent Technologies, Santa Clara, CA), with a choice of 32 amplifier outputs.

Then, the signal was directed to two phase detectors (CD-553R4, NF Corporation, Yokohama, Japan). These devices are composed of so-called lock-in amplifiers; thus, the precise amplitude could be measured even if the signal was very noisy.

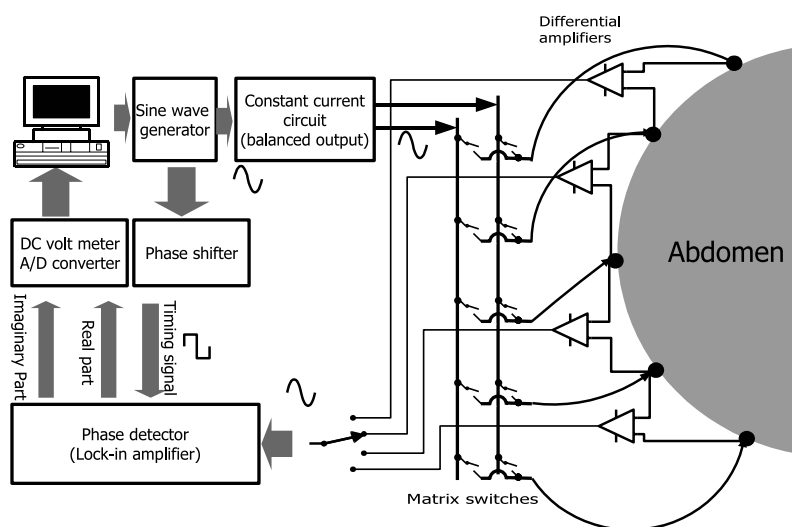


Figure 3. Schematic diagram of electronic circuits. Only five electrodes are shown.

Finally, those direct current signals transformed by the phase detectors were connected to a digital multimeter (Agilent34970A, Agilent Technologies, Santa Clara, CA). Thus, the voltages corresponding to complex bioimpedance could be measured and the data were acquired by the PC.

2.3. Control software

We developed software to control the device. The roles of the software were (1) control of air cylinders and air compressor to attach the electrodes onto the abdomen, (2) measurement and display of the subject's outline shape, cross-sectional area and waist circumference, (3) set up of measurement frequency and amplitude, (4) assignment of current electrodes corresponding to the measurement strategy, (5) measurement and display of complex voltage difference, (6) detection of abnormal data and re-measurement, (7) data saving and recall and (8) management of patient demographic data.

An operational panel was located on the PC screen and could be operated by mouse clicks. By means of those systems, operation for the measurement could be done by only one technician. The software was programmed with LabWindows/CVI (version 5.5, National Instruments Corporation, Austin, TX).

3. Method: imaging software

The apparatus described in the previous section provided impedance data for pairs of current electrodes and pairs of sense electrodes, both selected from 32 electrodes surrounding the patient's abdomen. Obviously, the data of adjacent current electrode pairs are the best for resolution but the worst for the signal-to-noise ratio (S/N). To balance the concerns of resolution and S/N, we chose 32 next adjacent current electrode pairs, and, for each pair, avoiding the current electrodes, obtained 28 adjacent sense electrode pairs, i.e. 32 times 28 equals 896 impedance data. For example, in the notation of electrode numbers increasing

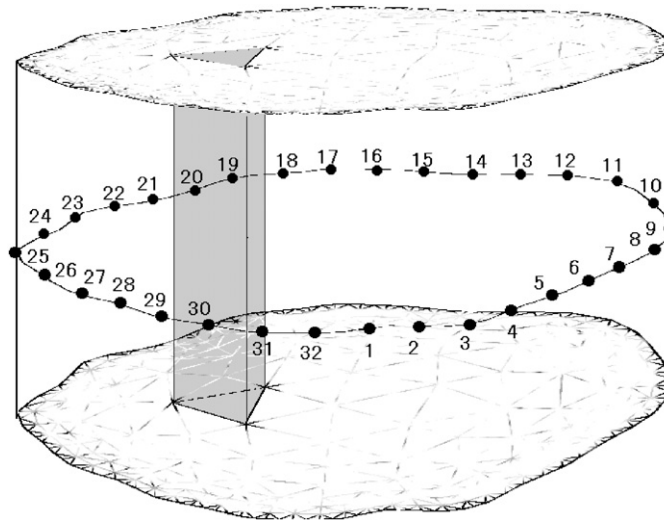


Figure 4. Schematic drawing of the model abdomen. Each of the triangular prisms was assumed to have the same conductivity.

counterclockwise as viewed from the top, the current electrode pair (1, 3) was combined with sense electrodes (4, 5), (5, 6), ..., (31, 32); the current electrode pair (2, 4) was combined with sense electrodes (5, 6), (6, 7), ..., (32, 1), and so on.

During the software development stage, we noticed that the observed impedance data itself were rather difficult to use for reliable calculation. We smoothed out the data based on certain natural physical principles, and further extended the smoothed data into a virtual 64-electrode system to obtain higher resolution near the surface.

In order to obtain a consistent conductivity distribution, we constructed a model abdomen of the same outline shape as subject's abdomen measured by the device with a certain height as in figure 4. The model height should be optimized compared with the subject's x-ray CT image but as a preliminary study, we chose twice the average diameter of the abdomen. The conductivity was assumed to be uniform in the heightwise (z) direction; for example, the gray area in figure 4 was assumed to have the same conductivity throughout. Only the upper half was calculated due to the mirror symmetry.

Based on this model, the forward problem, i.e. derivation of impedance data from the known cross-sectional distribution of the conductivity, was solved via the finite element method (FEM) as described later. The inverse problem, i.e. the optimization of conductivity distribution to reproduce the observed impedance data, was solved via the Marquardt method. Since the calculated distribution contained unwanted spatial high-frequency components, we had to filter them out.

Thus, the imaging process was as follows: (1) smoothing and extension of the impedance data, (2) solving the inverse problem to obtain the optimum conductivity distribution and (3) spatial filtering of the conductivity distribution.

3.1. Smoothing and extension of the impedance data

The observed data were found to have too much noise to use for image construction. It might be improved via repeated measurements and averaging, but that would be time consuming. Thus, we developed a smoothing method based on three physical principles.

- (A) The reciprocal theorem, i.e. interchange of current electrode pairs and sense electrode pairs does not change the impedance data.
- (B) The electric potential is either an increasing or decreasing smooth function of the distance between the current and sense electrodes.
- (C) If the distance between the current and sense electrodes is similar, i.e. the difference of electrode numbers is the same, the observed impedance is similar.

We denote electrode number i as increasing counterclockwise when viewed from the top. The current electrode pair m is defined as $i = m$ and $i = m + 2$, and the sense electrode pair n is defined as $i = n$ and $i = n + 1$. Here and from now on, in order to simplify the suffix notation, the modular arithmetic rule is applied to the electric pole numbers. The observed impedance is denoted as $Z_{m,n}^{(32)}$. The principle A is expressed as

$$Z_{m,n}^{(32)} + Z_{m,n+1}^{(32)} = Z_{n,m}^{(32)} + Z_{n,m+1}^{(32)}. \quad (1)$$

The principle B applies to the series $Z_{m,m+3}^{(32)}, Z_{m,m+4}^{(32)}, \dots, Z_{m,m-2}^{(32)}$, and as a result of A, also applies to the series $Z_{n+2,n}^{(32)}, Z_{n+3,n}^{(32)}, \dots, Z_{n-3,n}^{(32)}$. The principle C applies to the series $Z_{1,1+k}^{(32)}, Z_{2,2+k}^{(32)}, \dots, Z_{32,32+k}^{(32)}$, where $k = 3, 4, \dots, 31$. The data smoothing and extension procedure were as follows. Here we used only the real part of the impedance, which was treated as a positive real number.

In the actual measurement, we frequently encountered apparently abnormal data, which should be specially treated in the following process. The criterion for the abnormality was derived from principle C. Since the series data should be similar, the data should be in a certain range around the logarithmic average of the data. The admissible range was set to be from 0.1 times the average to 2.8 times the average.

As an application of principle B, the series of $\ln Z_{m,m+k}^{(32)}$ and the series of $\ln Z_{n+k,n}^{(32)}$, $k = 3, 4, \dots, 31$, were independently approximated as polynomials of k , and each $\ln Z_{m,n}^{(32)}$ was replaced with the average of the two independent approximations. Here, the polynomial degree was chosen to be 14. For this approximation process, when the data were abnormally small, the logarithmic function was replaced by a linear function of tangent line intersecting the logarithmic function curve at the lower threshold. When the exponential of the polynomial approximation (for $\ln Z_{m,n}^{(32)}$), the exponential function was replaced by a linear function of tangent line intersecting the exponential function curve at the upper threshold. Thus, we could minimize the effect of outliers.

Furthermore, in order to utilize the principle C, since the series $Z_{m,m+k}^{(32)}$ is a periodic function of m , we approximated $\ln Z_{m,m+k}^{(32)}$ as a sum of sinusoidal functions of m with period 32. The maximum degree of the sinusoidal function was chosen to be 8. Then, the first smoothing was executed again.

The smoothed impedance data $Z_{m,n}^{(32)}$ were summed up to the potential profile $U_m^{(32)}(s_i)$, $m = 1, 2, \dots, 32$; $i = m + 3, m + 4, \dots, m + 32$ for the unit current input, where s_i denotes the distance from one current electrode $m + 2$ to the electrode i along the model surface. The level of $U_m^{(32)}(s_i)$ was determined as the average for the same m being zero. The continuum profile $U_m^{(32)}(s)$ was then obtained as a polynomial approximation of degree 19, where the weighting factor was taken to be dU/ds . The potential of the intermediate between the current electrode and the nearest sense electrode was then replaced by an inversely proportional function to the distance from the current electrode. Thus, we obtained the 64-electrode system impedance $Z_{2m,n}^{(64)}$ for 32 current patterns $m = 1, 2, \dots, 32$. The following relations hold:

$$Z_{m,n}^{(32)} = Z_{2m,2n}^{(64)} + Z_{2m,2n+1}^{(64)}. \quad (2)$$

The impedance data of current patterns with odd number $2m + 1$ were interpolated utilizing the periodicity of $Z_{m,m+k}^{(64)}$, $m = 1, 2, \dots, 64$, i.e. approximated as a sum of the sinusoidal functions of m with period 64. The maximum degree of the sinusoidal function was chosen to be 15.

We obtained extended impedance data of 64 current patterns with 58 sense electrode pairs, or 3712 data in all. The principle A for a 64-electrode system is expressed as

$$Z_{m,n}^{(64)} + Z_{m,n+1}^{(64)} + Z_{m,n+2}^{(64)} + Z_{m,n+3}^{(64)} = Z_{n,m}^{(64)} + Z_{n,m+1}^{(64)} + Z_{n,m+2}^{(64)} + Z_{n,m+3}^{(64)}. \quad (3)$$

There are 1720 relations, which means that we can reduce the target impedance data for the inverse problem, if these relations really hold, but they actually do not hold because of noise and the smoothing process. In order to recover the reciprocal theorem, starting from the (m, n) pair of the farthest current and sense electrode, the deviation from this relation was modulated little by little (by 10% at each step, i.e. 5% of left-hand side minus right-hand side was subtracted from the left-hand side, and added to the right-hand side, maintaining the relative ratio of four terms). This process from the farthest current and sense electrode to the nearest one was repeated until convergence. As a minimum necessary set, we chose the target impedance data as

$$Z_{m,k} = Z_{2m,2m+2k+3}^{(64)} + Z_{2m,2m+2k+4}^{(64)}, \quad \text{where } m = 1, 2, \dots, 32; \quad k = 1, 2, \dots, 29. \quad (4)$$

These mutually independent 928 data contain the nearest current and sense electrode pairs in a 64-electrode system, which is sufficient for the fine resolution near the electrode, i.e. near the model surface. Because of the reciprocal theorem, this choice effectively contains part of the impedance data for the extended current patterns of odd number $2m + 1$.

3.2. Optimization of the conductivity distribution

The algorithm for the inverse problem of EIT has been studied extensively (Holder 2005b), but we used instead the standard algorithm of the nonlinear minimization method, namely, the Marquardt method (Yorkey *et al* 1987, Marquardt 1963). For our preliminary study, the modeling of electrode was simple as described in the next section, which was not so accurate as proposed in the work of Cheng *et al* (1989). Unifying the suffix of the impedance m, k into i , and denoting the calculated impedance data as Z_i , and experimental data as $Z_i^{(\text{Exp})}$, the residual was defined as

$$\Delta \ln Z_i = \ln Z_i^{(\text{Exp})} - \ln Z_i. \quad (5)$$

The error function Φ was expressed as

$$\Phi = \sum_i (\Delta \ln Z_i)^2. \quad (6)$$

We first defined the sensitivity matrix

$$S_{ij} = \partial \ln Z_i / \partial \ln \sigma_j, \quad (7)$$

where σ_j denoted the conductivity of the j th volume.

Denoting $\mathbf{E}_{m,j}$ and $\mathbf{E}_{n,j}$ as electric field vectors at the small volume dv_j in the j th volume, when the unit current is applied at the current electrode pair m and n , respectively, the sensitivity matrix $S_{i,j} = S_{(m,n),j}$ for the current electrode pair m and sense electrode pair n is calculated as (Yorkey *et al* 1987, Geselowitz 1971)

$$S_{i,j} = \frac{\sigma_j}{Z_i} \int \mathbf{E}_{m,j} \cdot \mathbf{E}_{n,j} dv_j. \quad (8)$$

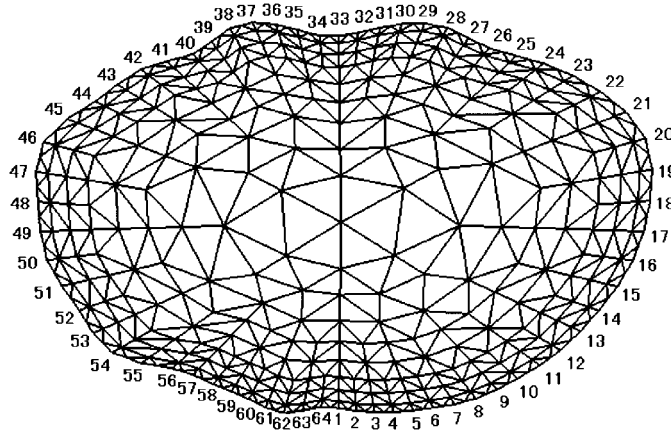


Figure 5. Discretization in the cross-section of the abdomen for the finite element method.

The Marquardt method is a procedure for iterative improvement of the trial solution σ_j to minimize Φ . The increment $\Delta \ln \sigma_j$ for the improvement of $\ln \sigma_j$ is calculated as a solution of

$$\sum_j \left\{ \sum_i S_{il} S_{ij} + \delta_{lj} \lambda \right\} \Delta \ln \sigma_j = \sum_i S_{il} \Delta \ln Z_i. \quad (9)$$

The selection of the parameter λ is essential to obtaining a stable solution. The meaning of λ is clarified via singular value decomposition of $S_{i,j}$. We denote the eigenvalue as D_k in the descending order, the left eigenvector in the $\Delta \ln Z_i$ space as $U^{(k)}$, and the right eigenvector in the $\Delta \ln \sigma_j$ space as $W^{(k)}$. D_k represents the independent mapping coefficient (sensitivity) from $W^{(k)}$ to $U^{(k)}$. Since small D_k represents the magnified effect of the small deviation in the $\Delta \ln Z_i$ space, it is necessary to discard the smaller eigenvalue mapping for a stable solution (Zadehkoochak *et al* 1991). It is easy to show that the effect of the k th eigenvector component of $\Delta \ln Z_i$ space is reduced by $D_k^2 / (D_k^2 + \lambda)$, which means that λ should be chosen with a certain ratio to D_1^2 . Thus we selected λ as

$$\lambda = \beta D_1^2 \quad (10)$$

and we initially chose $\beta = 0.3$ and decreased it gradually to 0.01 during the conversion process. Roughly speaking, 1/3 of the $\Delta \ln \sigma_j$ space was utilized when $\beta = 0.01$. Since D_1 did not change very much during the conversion process, it was enough to execute singular value decomposition at the first iteration or several times at most. When the singular value decomposition was executed, transforming the unknown to the eigenvector space, it was found to be possible to reduce the unknown of the simultaneous equation of the Marquardt method for the subsequent several iterations.

3.3. Discretization of the model and choice of independent unknowns

For the forward calculation using FEM, we discretized the cross-section containing electrodes into 708 triangles as in figure 5. The numbers denote the 64 electrodes. The center area was roughly discretized because the potential variation was expected to be small.

As for the z direction, the upper half volume was divided into 708 triangular prisms with bottom triangles, where the conductivity was assumed to be uniform. These triangular

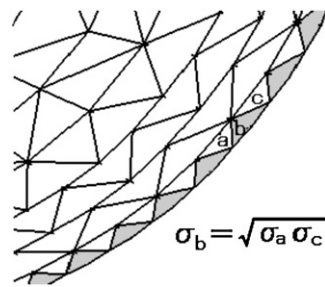


Figure 6. Discretization of conductivity distribution near the surface.

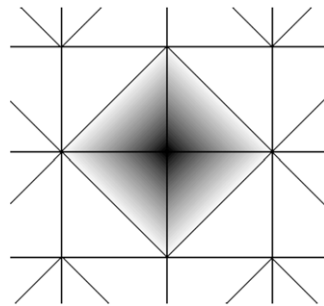


Figure 7. Current distribution near the current electrode.

prisms were further divided into 18 tetrahedral elements, the size of which increased with z . Thus, the total number of elements was 12 744, and that of nodes was 2933. Since conductivity distribution near the surface area was expected to have a small variation along the circumferential direction, we further reduced the number of independent unknown conductivities from 708 to 420 as in figure 6. (For the surface layer, the gray element's conductivity was assumed to be the geometric average of the adjacent white element's conductivity, and for the next three layers, most adjacent pairs were assumed to have the same conductivity.)

Since we extrapolated the voltage of the sense electrode nearest to the current electrode assuming inverse dependence on the distance from the nearest current electrode, the natural assumption for the Neumann boundary condition of the current electrode was a pyramidal shape distribution for the four surface elements containing electrode center node, as shown in figure 7.

3.4. Spatial filtering of the conductivity distribution

Spatial resolution of the conductivity distribution of the inverse problem depends on the choice of the parameter β in the previous section. However, high-frequency components of the image are very sensitive to the noise in the impedance data. Since we could neither analyze the nature of the noise nor trace their effect exactly, we had to filter out high-frequency components to obtain a reasonable image compared with an x-ray CT image. The choice of filtering functions and parameters are rather arbitrary, but from the viewpoint of sensitivity, it is natural that the length scale of the filtering function should be taken to be longer in the center compared to

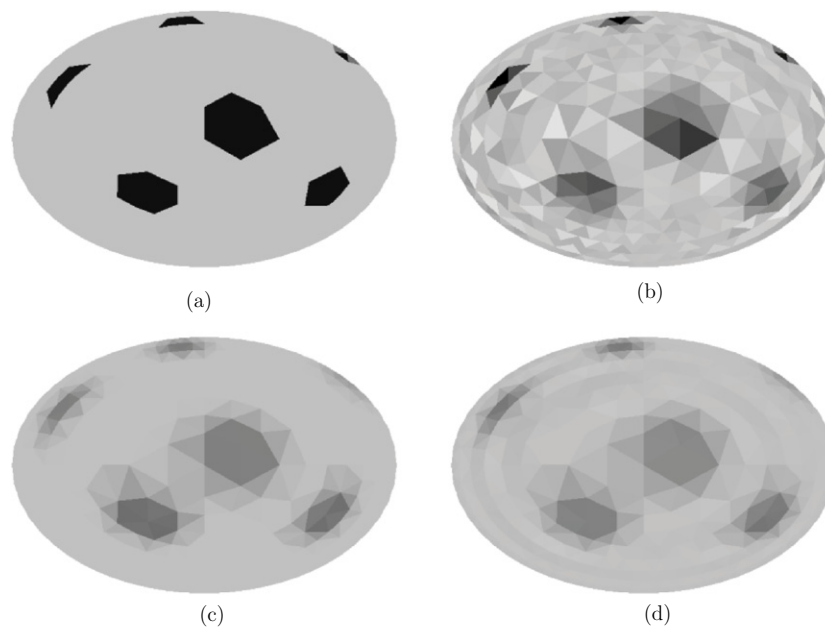


Figure 8. Simulation study of virtual objects with known conductivity and geometry. Target (left) and derived (right): raw image (upper) and filtered image (lower).

the area near the surface. Also, in terms of the surface area, the length scale of the filtering should be longer in the circumferential direction compared to the radial direction.

The detail of the filter process was described in the appendix. The length scale of the filtering function was $0.6r_b$ in the center, $(3/7)r_b$ in the radial direction on the surface, and $(6/7)\pi r_b$ in the circumferential direction on the surface. Here r_b denotes the radial coordinate on the circumference with the same angle coordinate of the filtering position.

3.5. Algorithm implementation

The algorithm previously described was integrated with an image reconstruction software. The software was programmed with a FORTRAN77 compiler. It took about 4 min to reconstruct an image using a conventional PC equipped 1.8 GHz Celeron[®] processor.

4. Results

4.1. Simulation study

To demonstrate the validity of the image reconstruction software, we did a simulation study. The conductivity distribution of the virtual model is shown in figure 8(a). We assigned conductivities of $4.0 \times 10^{-5} (\Omega \text{ mm})^{-1}$ and $4.0 \times 10^{-4} (\Omega \text{ mm})^{-1}$ for target objects and background, respectively. In the simulation study, an electric current was introduced through electrodes onto the virtual model with a known conductivity distribution, then the generated voltage differences between pairs of electrodes were computed using FEM.

The solution of the inverse problem derived by the image reconstruction software is shown in figure 8(b). Furthermore, smoothed images of both the target image and the image derived from the spatial smoothing filter are shown in figures 8(c) and (d).

The smoothed target model image and smoothed derived image were almost identical. Therefore, the fact that the software could solve the inverse problem in the resolution of the target image in figure 8(a) was demonstrated.

4.2. Human study

The subjects were the two authors, namely, TY and MK. TY is a lean type with a body mass index (BMI) of 19 kg m^{-2} . On the other hand, MK is an athletic type with a BMI of 23 kg m^{-2} . The probing current was 500 kHz in frequency and 1.0 mA in amplitude. Electrodes were covered with conductive gel and were attached onto subject's abdomen at the umbilical level. The measurement was carried on after a few minutes to wait for the relaxation of conductive resistance.

The probing current was sunk between the next adjacent electrodes; thus, using 29 electrodes, 28 adjacent voltage differences were measured. Then the pair of current electrodes was shifted, and voltage differences were measured in the same manner. Finally, all of the possible voltage differences were measured in 32 pairs of current electrodes. The measured data were monitored using three-dimensional plot on the PC screen throughout the measurements, and when obviously irregular data were found, the measurement was repeated manually. Total time to scan completely was about 4–8 min depending on how much re-measurements were made.

Figures 9(a) and (c) show reconstructed images by x-ray CT, and figures 9(b) and (d) show the EIT-reconstructed images with the common log-transformed conductivity expressed in colors. In the EIT images, the green region represents low conductivity, which may indicate body fat, and the red region represents high conductivity, which may indicate muscles.

Outlined shapes were slightly different in these two types of images, because the CT scan images were derived from the subjects in the supine position while the EIT images were derived in the upright position. In each EIT image, subcutaneous fat was imaged almost identical to the CT scan image. Furthermore, the muscles surrounding the viscera located inside the subcutaneous fat were also imaged. But visceral organs, vertebra and surrounding muscles were not sufficiently imaged.

5. Discussion

In the simulation study, data were generated using the FEM from a virtual model with known conductivity distribution. The reconstructed image from those data demonstrated the validity of the image reconstruction software. Consequently, human abdominal bioimpedances were measured using 32 electrodes, and we estimated the abdominal bioimpedance distribution using our image reconstruction software. From the image of bioimpedance distribution, we could obtain an image similar to an x-ray CT of the region of subcutaneous fat and the muscles surrounding the viscera.

We think the main reason for the good results was that the aim of the present study was focused on the distinction between body fat and other body tissues. Of course, the contrast in electric conductivity between the body fat and the other tissues is very large; thus, it is rather easy to distinguish them.

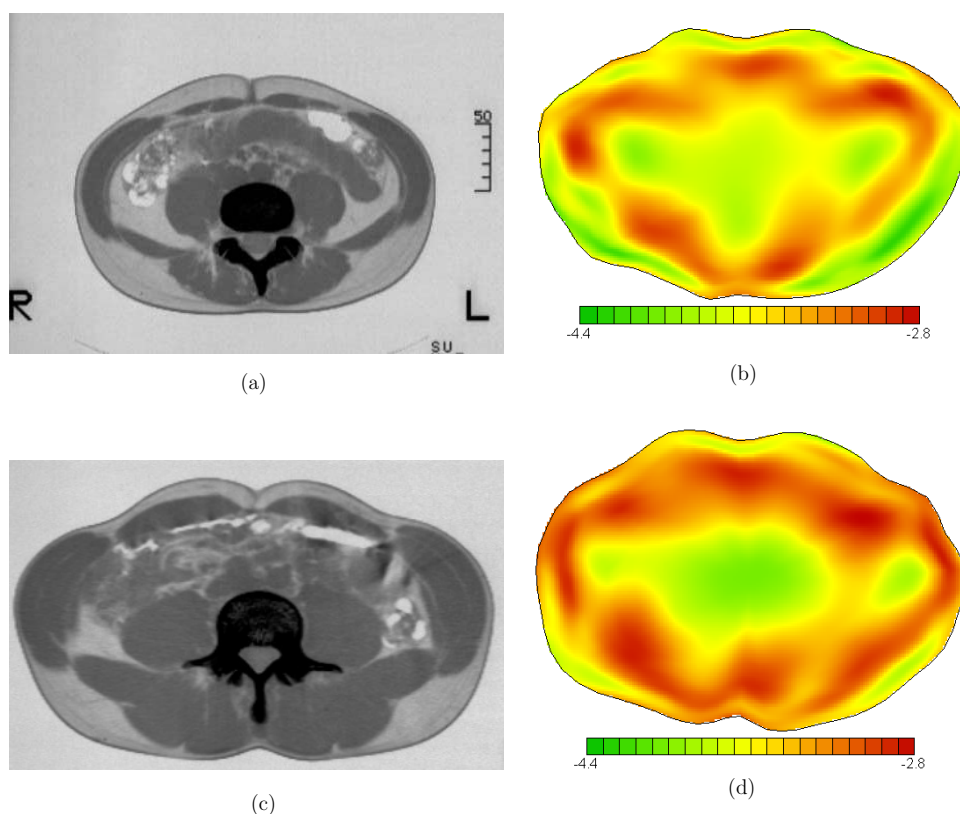


Figure 9. Reconstructed images: x-ray CT images (left); EIT images (right); subject TY (upper); subject MK (lower). Common log-transformed conductivity was imaged in color on the EIT images. The color scales are shown in terms of \log_{10} (conductivity in units $(\Omega \text{ mm})^{-1}$).

In terms of the device, we could point out several features, namely: (1) the probing current frequency was relatively high; (2) the electrodes were relatively numerous, and (3) the subject's outline shape was also measured.

Our preliminary study with several probing frequency ranging 50–500 kHz showed the image with 500 kHz was best of all in the quality (data not shown). We thought the high frequency was effective to overcome the electrical anisotropy of body tissues especially skeletal muscles. In the case of 50 kHz, which is frequently used to estimate body fat, the anisotropy in the result is large; thus, more parameters are needed to reconstruct the image with consideration of the anisotropy. By contrast, in the case of 500 kHz, which we used in the present study, the anisotropy might be small (Epstein and Foster 1983); thus, the image reconstruction is valid without consideration of anisotropy.

The reason for the 32 electrodes was that we found that 16 electrodes were too few to reconstruct the image in our preliminary study (data not shown). We think that 32 electrodes is a good number using the interpolation presented in this paper.

In most of the preceding studies, electrodes were manually attached (Nebuya *et al* 2006), a method that is very time-consuming; more importantly, the subject's body outline shape is not determined using this method. As a result, the derived image would be inaccurate because the shape was usually assumed to be a simple ellipse.

In terms of the image reconstruction software, we could point to several features, namely: (1) raw data were modified in conformity with the reciprocal theorem; (2) the number of data was expanded using interpolation; (3) to reduce the estimation parameters, we assumed homogeneity in the heightwise direction, and (4) to reduce the estimation parameters, we could neglect the electrical anisotropy of body tissue.

Full three-dimensional image reconstructions (Polydorides and Lionheart 2002) would be the ideal method if the accuracy of the measured bioimpedance and body outline shape were good enough, and the number of data was sufficient, but in the real world, these factors are limited. Therefore, the method presented in this paper was practically more appropriate than a method involving more estimation parameters, in consideration of the device capability. But if the capability of the device including the resolution of voltage measurement, the speed of the measurement and the stability of the measurement were increased, imaging the three-dimensional conductivity distributions would be essential.

The presented study was successful in part but did not achieve a sufficient quality of image for clinical use. From the EIT-reconstructed image, it is impossible to distinguish visceral fat from muscles such as the small intestine or large intestine in consideration of the mesh size. The x-ray CT image can make that distinction.

However, the estimation of visceral fat by x-ray CT was defined as a two-dimensional measure (Yoshizumi *et al* 1999), even though body fat is distributed three-dimensionally. Since the two-dimensional EIT image reflects an average with respect to the z direction, it might provide a more appropriate estimation of visceral fat than the x-ray CT image. In order to confirm this, a framework to estimate the measure of visceral fat from the two-dimensional conductivity image of an abdominal cavity, assuming an amalgam of fat and intestine, may be needed. That is our challenge for the future along with improvement of the reconstruction image.

6. Conclusion

We partially succeeded in human abdominal fat imaging utilizing EIT. Our results suggested that we will be able to develop a safe and practical abdominal fat scanner through future improvements.

Acknowledgments

The authors are employees of Kao Corporation and were funded by the company. The mechanical design and its assembly were performed by two engineers (T Ishikawa and K Iwane, Processing Development Research Laboratories, Kao Corporation). The authors thank them for their collaboration.

Appendix

Filtering procedure

The filtering procedure was a preliminary version used in this report. Since the scale of the filtering length should be related to the resolution of the tomography calculation, we mapped the original area into the surface of a sphere nonlinearly so as to reflect the resolution, i.e. high-resolution area was relatively extended on the sphere, and applied the same scale filter on the sphere. The details are described as follows.

First, the radial coordinate r in the model cross section including the electrodes was mapped into the radial coordinate ρ in a circle with a unit radius as

$$\rho = (S^{(\text{filter})}(r/r_b)^3 + (r/r_b))/(S^{(\text{filter})} + 1), \quad (\text{A.1})$$

where r_b denotes the radial coordinate on the circumference with the same-angle coordinate. The parameter $S^{(\text{filter})}$ is for the adjustment of the resolution ratio of the center and surface areas, which was chosen to be 2.0. Denoting the angle coordinate as θ , the Cartesian coordinates ξ and η are

$$\xi = \rho \cos \theta; \quad \eta = \rho \sin \theta. \quad (\text{A.2})$$

Next, the area in the circle was mapped on the sphere of radius $R^{(\text{sphere})}$, reserving the radius length. The circumference length was thus shortened by the ratio

$$R^{(\text{periph})} = (R^{(\text{sphere})}/\rho) \sin(\rho/R^{(\text{sphere})}). \quad (\text{A.3})$$

The parameter $R^{(\text{sphere})}$ was chosen to be $2/\pi$. We introduced a simple filter function $F(x)$ as follows:

$$F(x) = 1 - x^2/2 \quad \text{for} \quad x \leq \sqrt{2} \quad (\text{A.4})$$

$$F(x) = 0 \quad \text{for} \quad x > \sqrt{2} \quad (\text{A.5})$$

and the function of conductivity $f(\sigma_j)$ was filtered using parameter $R^{(\text{filter})}$ as

$$f_i^{\text{av}} = \left(\sum_j f(\sigma_j) F(\Delta_{ij}/R^{(\text{filter})}) A_j \right) / \left(\sum_j F(\Delta_{ij}/R^{(\text{filter})}) A_j \right), \quad (\text{A.6})$$

where A_j denotes the area of j th small element, and Δ_{ij} denotes the distance on the surface of a sphere

$$\Delta_{ij} = \sqrt{\Delta_\rho^2 + (R^{(\text{periph})} \Delta_\theta)^2}, \quad (\text{A.7})$$

$$\Delta_\rho = (\xi_i - \xi_j) \cos \theta_i + (\eta_i - \eta_j) \sin \theta_i, \quad (\text{A.8})$$

$$\Delta_\theta = -(\xi_i - \xi_j) \sin \theta_i + (\eta_i - \eta_j) \cos \theta_i. \quad (\text{A.9})$$

The filter length parameter $R^{(\text{filter})}$ was chosen to be 0.2. As a result, the length scale of the filtering function was $0.6r_b$ in the center, $(3/7)r_b$ in the radial direction on the surface and $(6/7)\pi r_b$ in the circumferential direction on the surface. The filtered conductivity distribution was obtained via inverse transformation of $f_i^{(\text{av})}$ as

$$\sigma_i^{\text{av}} = \text{inv} f(f_i^{\text{av}}). \quad (\text{A.10})$$

Since the filtering should conserve the averaged conductivity as a whole, we tested several forms of the function, and found that $f(x) = x^{1/6}$ was the best for our case, i.e. uniform in the z direction and having a random conductivity distribution with lognormal probability distribution. (It should be noted that $f(x) = x$ indicates a parallel register situation and that $f(x) = 1/x$ indicates a series register situation.)

References

Boone K, Barber D and Brown B 1997 Imaging with electricity: report of the European Concerted Action on Impedance Tomography *J. Med. Eng. Technol.* **21** 201–32

- Brenner D J and Hall E J 2007 Computed tomography—an increasing source of radiation exposure *N. Engl. J. Med.* **357** 2277–84
- Cheng K S, Isaacson D, Newell J C and Gisser D G 1989 Electrode models for electric current computed tomography *IEEE Trans. Biomed. Eng.* **36** 918–24
- Després J P and Lemieux I 2006 Abdominal obesity and metabolic syndrome *Nature* **444** 881–7
- Epstein B R and Foster K R 1983 Anisotropy in the dielectric properties of skeletal muscle *Med. Biol. Eng. Comput.* **21** 51–5
- Genton L, Hans D, Kyle U G and Pichard C 2002 Dual-energy x-ray absorptiometry and body composition: differences between devices and comparison with reference methods *Nutrition* **18** 66–70
- Geselowitz D B 1971 An application of electrocardiographic lead theory to impedance plethysmography *IEEE Trans. Biomed. Eng.* **18** 38–41
- Grundey S M *et al* 2005 Diagnosis and management of the metabolic syndrome: an american heart association/national heart, lung, and blood institute scientific statement *Circulation* **112** 2735–52
- Holder D S (ed) 2005a *Electrical Impedance Tomography: Methods, History and Applications* (London: Institute of Physics Publishing)
- Holder D S (ed) 2005b The reconstruction problem *Electrical Impedance Tomography: Methods, History and Applications* (London: Institute of Physics Publishing) pp 3–64 chapter 1
- Klein S, Allison D B, Heymsfield S B, Kelley D E, Leibel R L, Nonas C and Kahn R 2007 Waist circumference and cardiometabolic risk: a consensus statement from Shaping America's Health: Association for Weight Management and Obesity Prevention; NAASO, The Obesity Society; the American Society for Nutrition; and the American Diabetes Association *Diabetes Care* **30** 1647–52
- Kohro T, Furui Y, Mitsutake N, Fujii R, Morita H, Oku S, Ohe K and Nagai R 2008 The Japanese National Health Screening and Intervention Program Aimed at Preventing Worsening of the Metabolic Syndrome *Int. Heart J.* **49** 193–203
- Kushner R F 1992 Bioelectrical impedance analysis: a review of principles and applications *J. Am. Coll. Nutr.* **11** 199–209
- Marquardt D 1963 An algorithm for least-squares estimation of nonlinear parameters *J. Soc. Ind. Appl. Math.* **11** 431–41
- Matsuzawa Y 2005 Metabolic syndrome—definition and diagnostic criteria in Japan *J. Atheroscler. Thromb.* **12** 301
- Nebuya S, Noshiro M, Yonemoto A, Tateno S, Brown B H, Smallwood R H and Milnes P 2006 Study of the optimum level of electrode placement for the evaluation of absolute lung resistivity with the Mk3.5 EIT system *Physiol. Meas.* **27** S129–37
- Polydorides N and Lionheart W 2002 A Matlab toolkit for three-dimensional electrical impedance tomography: a contribution to the electrical impedance and diffuse optical reconstruction software project *Meas. Sci. Technol.* **13** 1871–83
- Ryo M *et al* 2005 A new simple method for the measurement of visceral fat accumulation by bioelectrical impedance *Diabetes Care* **28** 451–3
- Scharfetter H, Brunner P, Mayer M, Brandstätter B and Hinghofer-Szalkay H 2005 Fat and hydration monitoring by abdominal bioimpedance analysis: data interpretation by hierarchical electrical modeling *IEEE Trans. Biomed. Eng.* **52** 975–82
- Scharfetter H, Schlager T, Stollberger R, Felsberger R, Hutten H and Hinghofer-Szalkay H 2001 Assessing abdominal fatness with local bioimpedance analysis: basics and experimental findings *Int. J. Obes. Relat. Metab. Disord.* **25** 502–11
- Watson S, Blundell H L, Evans W D, Griffiths H, Newcombe R G and Rees D A 2009 Can abdominal bioelectrical impedance refine the determination of visceral fat from waist circumference? *Physiol. Meas.* **30** N53–8
- Yorkey T J, Webster J G and Tompkins W J 1987 Comparing reconstruction algorithms for electrical impedance tomography *IEEE Trans. Biomed. Eng.* **34** 843–52
- Yoshizumi T *et al* 1999 Abdominal fat: standardized technique for measurement at CT *Radiology* **211** 283–6
- Zadehkochak M, Blott B, Hames T and George R 1991 Spectral expansion analysis in electrical impedance tomography *J. Phys. D: Appl. Phys.* **24** 1911–16